applied optics

Neural network method to correct bidirectional effects in water-leaving radiance

YONGZHEN FAN,[1,*] WEI LI,[1] KENNETH J. VOSS,[2] CHARLES K. GATEBE,[3] AND KNUT STAMNES[1]

[1]Light & Life Laboratory, Department of Physics and Engineering Physics, Stevens Institute of Technology, Hoboken, New Jersey 07307, USA
[2]Physics Department, University of Miami, Coral Gables, Florida 33124, USA
[3]NASA's Goddard Space Flight Center, Greenbelt, Maryland 20771, USA
*Corresponding author: yfan@stevens.edu

Received 20 July 2015; revised 13 November 2015; accepted 16 November 2015; posted 17 November 2015 (Doc. ID 246332); published 18 December 2015

Ocean color algorithms that rely on "atmospherically corrected" nadir water-leaving radiances to infer information about marine constituents such as the chlorophyll concentration depend on a reliable method to convert the angle-dependent measured radiances from the observation direction to the nadir direction. It is also important to convert the measured radiances to the nadir direction when comparing and merging products from different satellite missions. The standard correction method developed by Morel and coworkers requires knowledge of the chlorophyll concentration. Also, the standard method was developed based on the Case 1 (open ocean) assumption, which makes it unsuitable for Case 2 situations such as turbid coastal waters. We introduce a neural network method to convert the angle-dependent water-leaving radiance (or the corresponding remote sensing reflectance) from the observation direction to the nadir direction. This method relies on neither an "atmospheric correction" nor prior knowledge of the water constituents or the inherent optical properties. It directly converts the remote sensing reflectance from an arbitrary slanted viewing direction to the nadir direction by using a trained neural network. This method is fast and accurate, and it can be easily adapted to different remote sensing instruments. Validation using NuRADS measurements in different types of water shows that this method is suitable for both Case 1 and Case 2 waters. In Case 1 or chlorophyll-dominated waters, our neural network method produces corrections similar to those of the standard method. In Case 2 waters, especially sediment-dominated waters, a significant improvement was obtained compared to the standard method.

OCIS codes: (010.4450) Oceanic optics; (010.5620) Radiative transfer; (280.0280) Remote sensing and sensors; (290.1483) BSDF, BRDF, and BTDF.

http://dx.doi.org/10.1364/AO.55.000010

1. INTRODUCTION

The water-leaving radiance (L_w) and the corresponding remote sensing reflectance (R_{rs}), defined as $R_{rs} = L_w/E_d^{0+}$, where E_d^{0+} is the downward irradiance just above the ocean surface, are standard products in most operational ocean color algorithms from which other ocean color products, such as the chlorophyll-*a* concentration (CHL-*a*) or inherent optical properties (IOPs) of the water are derived. Hence, the accuracy of the water-leaving radiance or the remote sensing reflectance is of great importance to obtaining reliable ocean color products.

The water-leaving radiance (L_w) is the upward radiance in the water that is transmitted through the water–air interface. When attenuated direct sunlight and diffuse skylight penetrate the water–air interface and propagate into the water, some of the light will be scattered by seawater and its embedded constituents and propagate in the upward direction. A fraction of that light will eventually be transmitted through the water–air interface and leave the ocean. This fraction is known as the "water-leaving radiance". Therefore, the water-leaving radiance depends on: (i) illumination conditions at the ocean surface [e.g., clouds and aerosols will attenuate direct sunlight and reduce the magnitude and change the angular distribution of the diffuse radiation (skylight) reaching the ocean surface]; (ii) the optical properties of the water, especially the scattering by particles embedded in the water since scattering by pure water is nearly isotropic; and (iii) the sun-sensor geometry, i.e., the solar zenith angle θ_0, the viewing zenith angle θ (the corresponding angle in the water is θ'), and the relative azimuth angle between the sun and the viewing direction ($\Delta\phi$) as illustrated in Fig. 1. The concept of a normalized water-leaving radiance (nL_w) was introduced by Gordon and Clark [1] as the radiance that would be obtained if the Sun were at zenith ($\theta_0 = 0°$), the atmosphere

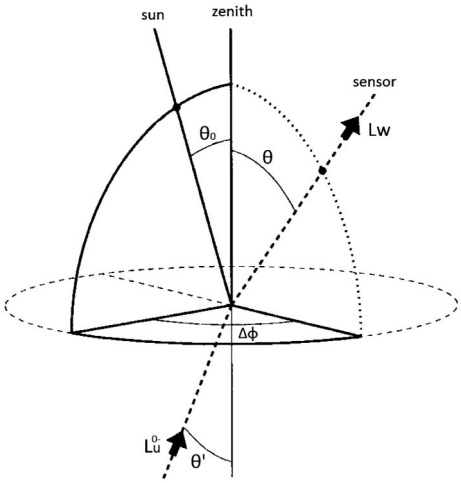

Fig. 1. Schematic illustration of the sun-sensor geometry.

absent, and the sensor looking at nadir ($\theta = 0°$). Clearly, the dependence on geometry has been removed in the normalized water-leaving radiance by fixing the position of the sun and the sensor, and assuming a black sky removes the dependence on illumination as well. Hence, the normalized water-leaving radiance nL_w and its associated remote-sensing reflectance nR_{rs} depend only on the properties of the water and can be directly used to derive ocean color products. Standard ocean color algorithms rely on an imperfect "atmospheric correction" to remove the influence of the atmosphere in order to infer the water-leaving radiance $L_w(\lambda, \theta_0, \theta, \Delta\phi)$ and its nadir counterpart $L_w(\lambda, \theta_0)$, where λ is the wavelength. Note that $L_w(\lambda, \theta_0)$ and its associated remote sensing reflectance $R_{rs}(\lambda, \theta_0)$ depend on the solar zenith angle θ_0, and is therefore apart from the imperfect atmospheric correction and different from the "ideal" nL_w and nR_{rs}. In this paper, we will focus on the remote-sensing reflectance at nadir, $R_{rs}(\lambda, \theta_0, \tau_a, \text{IOP}) \equiv R_{rs}(\lambda, \theta_0, \theta = 0, \tau_a, \text{IOP})$, and its angle-dependent counterpart, $R_{rs}(\lambda, \theta_0, \theta, \Delta\phi, \tau_a, \text{IOP})$, where τ_a and IOP are used to indicate that R_{rs} depends on the optical properties of the atmosphere, signified by τ_a, as well as those of the water, signified by IOP.

The dependence of $R_{rs}(\lambda, \theta_0, \theta, \Delta\phi, \tau_a, \text{IOP})$ on the geometry, referred to as the bidirectional reflectance distribution function (BRDF), is caused primarily by the anisotropy of the scattering phase function of the particles embedded in the water. The BRDF has been studied extensively in the past few decades, because satellite sensors do not measure the nadir water-leaving radiance directly. Therefore, a method to derive the nadir water-leaving radiance from the angle-dependent water-leaving radiance is required. Morel and Gentili [2–4] published a series of papers on this topic in the 1990s and showed that the remote sensing reflectance just above the ocean surface (0^+) at any geometry can be approximated by

$$R_{rs}(0^+, \theta_0, \theta, \Delta\phi, \tau_a, W, \text{IOP}, \lambda) = \Re(\theta_0, \theta', W, \lambda) \times \frac{f(\theta_0, \tau_a, W, \text{IOP}, \lambda)}{Q(\theta_0, \theta', \Delta\phi, \tau_a, W, \text{IOP}, \lambda)} \left[\frac{b_b(\lambda)}{a(\lambda)}\right], \quad (1)$$

where the angles θ_0, θ, and $\Delta\phi$ are given in Fig. 1 and W is the wind speed. In general, the wind speed is required because the BRDF depends also on surface roughness, which may be parameterized in terms of the wind speed [5]. The dimensionless function $\Re$ merges all the refraction and reflection effects when downward and upward radiances propagate through the water–air interface. The function f relates the irradiance reflectance ($R = E_u/E_d$) to the IOPs; the function Q is a bidirectional function, defined as $Q(\theta_0, \theta', \Delta\phi) = E_u^{0^-}/L_u^{0^-}(\theta_0, \theta', \Delta\phi)$. In 2002, Morel *et al.* [6] proposed an algorithm (denoted by MAG02 in this paper) to derive the nadir remote sensing reflectance $R_{rs}(0^+, \theta_0, \theta = 0, \tau_a, \text{IOP})$ as well as the normalized remote sensing reflectance $R_{rs}(0^+, \theta_0 = 0, \theta = 0, \tau_a = 0, \text{IOP})$ from the angle-dependent remote sensing reflectance $R_{rs}(0^+, \theta_0, \theta, \Delta\phi, \tau_a \approx 0, W, \text{IOP}, \lambda)$ using a lookup table that takes the three geometry angles and the chlorophyll-*a* concentration as input (here, $\tau_a \approx 0$ is used to remind us that an imperfect atmospheric correction has been used to derive the remote sensing reflectance from the measured top-of-the-atmosphere radiance). The MAG02 algorithm has been widely used in current ocean color algorithms as a standard correction method and it works well in open ocean (Case 1) water [7] in which the IOPs can be characterized in terms of the chlorophyll-*a* concentration. However, many areas of the ocean, especially coastal waters, cannot be classified as Case 1 due to the complexity of the water. These waters are therefore referred to as Case 2 waters. Many instruments are located in Case 2 water areas such as the AERONET-OC network, which was designed to provide validation data for ocean color products. The MAG02 algorithm is not suitable for Case 2 waters and larger uncertainties are observed in the nadir remote sensing reflectance when this method is applied to Case 2 waters [8].

Several attempts have been made to develop a BRDF correction method that can be applied to Case 2 waters. The basic idea is to merge the three functions $\Re$, f, and Q in Eq. (1) into one generalized function, $\mathcal{F}$, that only varies with geometry for given values of the IOPs. Lee *et al.* [9] proposed an algorithm to derive nadir remote sensing reflectance, $R_{rs}(\lambda_i, \theta_0)$, from the angular remote sensing reflectance, $R_{rs}(\lambda_i, \theta_0, \theta, \Delta\phi)$. The Lee *et al.* algorithm is based on the assumptions that the remote sensing reflectance can be written as a product of a function of the water IOPs expressed as Func(IOP) and a function G as follows:

$$R_{rs}(\lambda_i, \theta_0, \theta, \Delta\phi) = G(\lambda_i, \theta_0, \theta, \Delta\phi) \times \text{Func(IOP)}, \quad (2)$$

where the generalized function G was generated from Hydrolight radiative transfer simulations using a large set of different water IOPs, and therefore it also depends on water IOPs. The algorithm first derives the water IOPs from $R_{rs}(\lambda_i, \theta_0, \theta, \Delta\phi)$ using a quasi-analytical algorithm and determines the function G that best fits $R_{rs}(\lambda_i, \theta_0, \theta, \Delta\phi)$. In a second step, $R_{rs}(\lambda_i, \theta_0)$ was derived from the retrieved water IOPs and the value of the function G evaluated in the nadir direction, namely G_0. Gilerson *et al.* [10] proposed a similar algorithm, except that they first derive the single backscattering albedo, $\omega(\lambda_i) = b_b(\lambda_i)/[a(\lambda_i) + b_b(\lambda_i)]$, from $R_{rs}(\theta_0, \theta, \Delta\phi, \lambda_i)$ and then use a function $\alpha(\lambda_i, \theta_0, \theta, \Delta\phi, \omega_i)$ obtained from radiative transfer simulations to derive $R_{rs}(\lambda_i, \theta_0)$. Both algorithms operate on a wavelength by wavelength basis, and both achieved

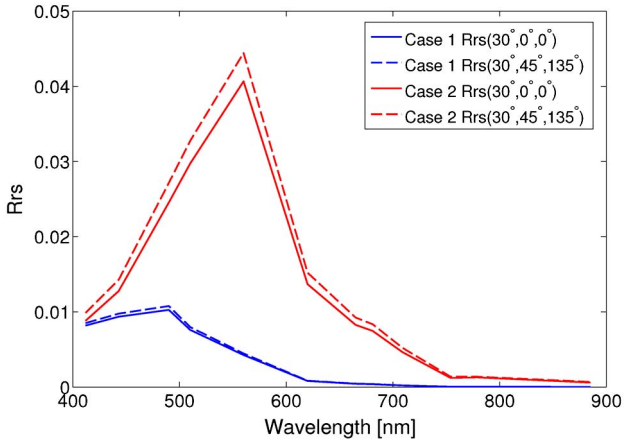

Fig. 2. Simulated remote sensing reflectance (R_{rs}) of two cases, blue lines (bottom) for Case 1 water and red lines (top) for Case 2 water. Solid lines are normalized remote sensing reflectances and dashed lines are angular remote sensing reflectances.

improvements over the MAG02 method when applied to Case 2 waters.

In this paper, we develop a neural-network-based algorithm that directly derives the entire spectral nadir remote sensing reflectance $R_{rs}(\lambda_i, \theta_0)$ from the angular value $R_{rs}(\lambda_i, \theta_0, \theta, \Delta\phi)$, without any prior knowledge of the water IOPs. Figure 2 shows two cases of simulated remote sensing reflectance, one for Case 1 water and one for Case 2 water. The difference in remote sensing reflectance between Case 1 and Case 2 waters is significant but, for each case, the difference is small between nadir remote sensing reflectance $R_{rs}(\lambda_i, \theta_0)$ and angular remote sensing reflectance $R_{rs}(\lambda_i, \theta_0, \theta, \Delta\phi)$. The spectral shape of the remote sensing reflectance is important because it reflects the water and atmospheric IOPs. Hence, for a specific set of water and atmospheric IOPs, there should be a relation between the spectrum of $R_{rs}(\lambda_i, \theta_0, \theta, \Delta\phi)$ and $R_{rs}(\lambda_i, \theta_0)$. In other words, the spectral nadir reflectance $R_{rs}(\lambda_i, \theta_0)$ can be expressed as a function of $R_{rs}(\lambda_i, \theta_0, \theta, \Delta\phi)$:

$$R_{rs}(\lambda_i, \theta_0) = \frac{\Re_0}{\Re}\frac{f_0}{f}\frac{Q}{Q_0}R_{rs}(\lambda_i, \theta_0, \theta, \Delta\phi), \quad (3)$$

where $\Re$, f, and Q are the functions appearing in Eq. (1) and $\Re_0$, f_0, and Q_0 are the values of the three functions evaluated in the nadir direction. Our goal is to establish a direct connection between $R_{rs}(\lambda, \theta_0, \theta, \Delta\phi)$ and $R_{rs}(\lambda_i, \theta_0)$. To achieve this goal, we simulated $R_{rs}(\lambda, \theta_0, \theta, \Delta\phi)$ and $R_{rs}(\lambda_i, \theta_0)$ for a wide range of water and atmospheric IOPs. Using this synthetic dataset, we then trained a neural network to establish a direct connection between $R_{rs}(\lambda, \theta_0, \theta, \Delta\phi)$ and $R_{rs}(\lambda_i, \theta_0)$ for any combination of water and atmospheric IOPs available in the synthetic dataset. We have found that a radial basis function neural network [11] is suitable to achieve our goal. Our algorithm takes $R_{rs}(\lambda, \theta_0, \theta, \Delta\phi)$ values for a desired set of wavelengths as input to achieve maximum accuracy. If a different set of wavelengths is desired, one can easily retrain the neural network.

2. NEURAL NETWORK METHOD

A. Water-Leaving Radiance Simulation

The water-leaving radiance or remote sensing reflectance can be simulated by solving the radiative transfer equation. In our study, we used AccuRT, which is a radiative transfer model (RTM) for the coupled atmosphere-ocean system based on the discrete-ordinate method [12–16]. AccuRT is an accurate, well-tested, and reliable RTM for the coupled system. We used a 13-layer atmosphere in AccuRT with a total height of 70 km, based on the U.S. Standard atmosphere profile. The IOPs of the atmospheric gas absorption were computed from a band model [17]. The scattering phase function for atmospheric molecules is the Rayleigh phase function. Aerosols were added to the bottom 2 km of the atmosphere. We used the set of aerosol models proposed by Ahmad *et al.* [18] based on AERONET observations. There are 80 different aerosol models that vary with the fraction of small aerosol particles (f_a) and relative humidity. This set of aerosol models is currently implemented in NASA's ocean color processing package SeaDAS. For the ocean, we implemented a 100 m deep homogeneous layer, and we assumed two types of embedded particles in the water, algal particles and nonalgal particles. In addition to particles, we also added colored dissolved organic matter in the water. The absorption and scattering coefficients and the scattering phase functions of pure water and embedded particles (see Fig. 3) are discussed in detail in Section 2.B.

The water-leaving radiance can be written as [4]

$$L_w(\lambda, \theta, \Delta\phi) = L_u(0^-, \lambda, \theta', \Delta\phi)\frac{[1-\rho(\lambda, \theta', \theta)]}{n(\lambda)^2}, \quad (4)$$

where $L_u(0^-, \lambda, \theta', \Delta\phi)$ is the upwelling radiance just below the ocean surface, $\rho(\lambda, \theta', \theta)$ is the Fresnel reflectance, and $n(\lambda)$ is the refractive index of water. The term $\frac{[1-\rho(\lambda,\theta',\theta)]}{n(\lambda)^2}$ is the transmittance of the water–air interface when light propagates from water to air. In the nadir direction, the transmittance is frequently approximated as a constant (0.54). However, recent studies have shown that this value is not always valid and a comprehensive study of the transmittance at non-nadir directions is underway [19]. In our study, we use a different approach. To obtain the water-leaving radiance, we computed the upward radiance just above the ocean surface twice using AccuRT. Assuming the ocean to be black, i.e., totally absorbing (no scattering), we first computed the upward radiance just above the ocean surface, $L_{u,\text{black}}(0^+, \lambda, \theta_0, \theta, \Delta\phi)$, which includes the radiance due to Fresnel reflection of direct attenuated sunlight and skylight by the water–air interface but no radiance from the water. The second time, we included the ocean with water and its embedded constituents and computed the radiance $L_u(0^+, \lambda, \theta_0, \theta, \Delta\phi)$, which included the water-leaving radiance as well as the Fresnel reflected direct attenuated sunlight and skylight. Then the water-leaving radiance was computed from the difference

$$L_w(0^+, \lambda, \theta_0, \theta, \Delta\phi) = L_u(0^+, \lambda, \theta_0, \theta, \Delta\phi) - L_{u,\text{black}}(0^+, \lambda, \theta_0, \theta, \Delta\phi). \quad (5)$$

B. Water IOP Model

The total IOPs of the water, i.e., the total absorption coefficient $a_t(\lambda)$ and the total scattering coefficient $b_t(\lambda)$, are due to

contributions from pure water, embedded particles, and colored dissolved organic matter:

$$a_t(\lambda) = a_w(\lambda) + a_p(\lambda) + a_{\mathrm{CDOM}}(\lambda). \quad (6)$$

$$b_t(\lambda) = b_w(\lambda) + b_p(\lambda). \quad (7)$$

For pure water, we use the absorption coefficient $a_w(\lambda)$ based on data published by Pope and Fry (1997) [20] for wavelengths between 400 and 700 nm, and by Kou *et al.* [21] for wavelengths between 720 and 900 nm. Pure water-scattering coefficients $b_w(\lambda)$ are based on published data [22] and the Rayleigh scattering phase function is given by [22]:

$$p(\cos\Theta) = \frac{3}{3+f}(1 + f\cos^2\Theta), \quad (8)$$

where $f = \frac{1-\rho}{1+\rho}$ and ρ is the depolarization ratio attributed to the anisotropy of the scatterer, which was set to be $\rho = 0.0899$.

The IOPs of the water constituents are usually derived from a bio-optical model. In our study, we assumed that there are two types of embedded particles in the water: (i) algal particles (denoted by CHL), and (ii) nonalgal particles (denoted by MIN), in addition to the colored dissolved organic matter (CDOM). We used the CoastColor Round Robin (CCRR) bio-optical model [23].

The absorption coefficient of the algal particles is given by a nonlinear function of the Chlorophyll-*a* concentration (CHL) [24]:

$$a_{\mathrm{CHL}}(\lambda) = A(\lambda) \times \mathrm{CHL}^{E(\lambda)}, \quad (9)$$

where $A(\lambda)$ and $E(\lambda)$ are given by Bricaud *et al.* [24]. The beam attenuation coefficient for algal particles at 660 nm is given by [25]:

$$c_{\mathrm{CHL}}(660) = 0.407 \times \mathrm{CHL}^{0.795}, \quad (10)$$

and the spectral variation is taken to be [6]:

$$c_{\mathrm{CHL}}(\lambda) = c_{\mathrm{CHL}}(660) \times (\lambda/660)^{\eta}, \quad (11)$$

where

$$\begin{array}{ll} \eta = 0.5 \times [\log_{10}\mathrm{CHL} - 0.3] & 0.02 < \mathrm{CHL} < 2.0 \\ \eta = 0 & \mathrm{CHL} \geq 2.0 \end{array}.$$

The spectral variation of the scattering coefficients for the algal particles is given by the difference between the beam attenuation and absorption coefficients:

$$b_{\mathrm{CHL}}(\lambda) = c_{\mathrm{CHL}}(\lambda) - a_{\mathrm{CHL}}(\lambda). \quad (12)$$

The scattering phase function for the algal particles is assumed to be described by the Fournier–Forand phase function [26,27] (see Fig. 3):

$$p_{\mathrm{FF}}(\cos\Theta) = \frac{1}{4\pi(1-\delta)^2\delta^{\nu}}\{\nu(1-\delta) - (1-\delta^{\nu}) + \frac{4}{u^2}[\delta(1-\delta^{\nu}) - \nu(1-\delta)]\} + \frac{1-\delta_{180}^{\nu}}{16\pi(\delta_{180}-1)\delta_{180}^{\nu}}[3\cos^2\Theta - 1], \quad (13)$$

where $\nu = 0.5(3-\gamma)$, and γ is the slope of the particle size distribution function (assumed to be a Junge or power law distribution), which typically varies between 3.0 and 5.0; $u = 2\sin(\Theta/2)$, $\delta \equiv \delta(\Theta) = \frac{u^2}{3(m-1)^2}$, $\delta_{180} = \delta(\Theta = 180°) = \frac{4}{3(m-1)^2}$, Θ is the scattering angle, and m is the refractive index. In a previous study, Li *et al.* [28] used $m = 1.0686$ and $\gamma = 3.38$, which correspond to a backscattering ratio of 0.0056. As noted by Mobley *et al.* [27], this choice of $[m, \gamma]$ values is consistent with a certain mixture of living microbes.

The absorption coefficient of the nonalgal particles at 443 nm is given by [29]:

$$a_{\mathrm{MIN}}(443) = 0.031 \times \mathrm{MIN}, \quad (14)$$

and the spectral variation can be written as [29]

$$a_{\mathrm{MIN}}(\lambda) = a_{\mathrm{MIN}}(443)\exp[-0.0123(\lambda - 443)]. \quad (15)$$

The scattering coefficient of the nonalgal particles at 555 nm is given by [30]:

$$b_{\mathrm{MIN}}(555) = 0.51 \times \mathrm{MIN}, \quad (16)$$

and the spectral variation of the beam attenuation coefficients of the nonalgal particles is given by [30]:

$$c_{\mathrm{MIN}}(\lambda) = c_{\mathrm{MIN}}(555) \times (\lambda/555)^{-0.3749}, \quad (17)$$

where

$$c_{\mathrm{MIN}}(555) = a_{\mathrm{MIN}}(555) + b_{\mathrm{MIN}}(555) = 0.52 \times \mathrm{MIN}.$$

The spectral variation of the scattering coefficients for the nonalgal particles is given by the difference between the beam attenuation and absorption coefficients:

$$b_{\mathrm{MIN}}(\lambda) = c_{\mathrm{MIN}}(\lambda) - a_{\mathrm{MIN}}(\lambda). \quad (18)$$

The average Petzold phase function [31] with a backscattering ratio of 0.019, as tabulated by Mobley [32], is used to describe the scattering phase function for nonalgal particles.

The total IOPs due to embedded particles are given by:

$$a_p(\lambda) = a_{\mathrm{CHL}}(\lambda) + a_{\mathrm{MIN}}(\lambda), \quad (19)$$

$$b_p(\lambda) = b_{\mathrm{CHL}}(\lambda) + b_{\mathrm{MIN}}(\lambda). \quad (20)$$

The spectral variation of the CDOM absorption is given by an exponentially decreasing function [29]:

$$a_{\mathrm{CDOM}}(\lambda) = \mathrm{CDOM} \times \exp[-0.0176(\lambda - 443)], \quad (21)$$

where CDOM means the CDOM absorption at 443 nm.

The moment-fitting method of Hu *et al.* [33] was used to compute Legendre expansion coefficients $\chi_{\ell,\mathrm{PET}}$ and $\chi_{\ell,\mathrm{FF}}$ for the Petzold and FF scattering phase functions. The total scattering phase function Legendre expansion coefficients χ_{ℓ} are given by

$$\chi_{\ell} = f_{\mathrm{FF}} \times \chi_{\ell,\mathrm{FF}} + f_{\mathrm{PET}} \times \chi_{\ell,\mathrm{PET}} + (1 - f_{\mathrm{FF}} - f_{\mathrm{PET}}) \times \chi_{\ell,\mathrm{water}}, \quad (22)$$

where f_{FF} and f_{PET} are the fractions of particles that scatter according to the FF and Petzold phase functions defined as $f_{\mathrm{FF}} = b_{\mathrm{CHL}}/b_t$ and $f_{\mathrm{PET}} = b_{\mathrm{MIN}}/b_t$.

C. Neural Network Training

The radial basis function (RBF) neural network is an artificial neural network that uses RBFs as neurons and can be used in a wide range of applications [34]. The neural network needs to be properly trained in order to work satisfactorily. During the training, the neural network learns the pattern of the

relation between the input and output dataset. We generated a training dataset from our RTM, AccuRT. This training dataset contains 30,000 data points of $L_u(0^+, \theta_0, \theta, \Delta\phi)$ and $L_{u,\text{black}}(0^+, \theta_0, \theta, \Delta\phi)$ at seven wavelengths—412, 443, 490, 510, 560, 620, and 665 nm—which are similar to the wavelengths used in the MAG02 algorithm. The synthetic dataset was generated in the following manner. First, we randomly selected 5000 combinations of the aerosol optical depths at 865 nm ($\tau_a(865)$), fraction of the small aerosol particles (f_a), relative humidity, and three ocean parameters: CHL, MIN, and CDOM. In order to cover a wide range of water and atmospheric IOPs, these six parameters were randomly sampled from the following ranges in logarithmic space:

1. $\tau_a(865)$: 0.001—0.5,
2. f_a: 1—95 [%],
3. RH: 30—95 [%],
4. CHL: 0.01–100 [mg · m^{-3}],
5. MIN: 0.01–100 [g · m^{-3}],
6. CDOM: 0.001–10 [m^{-1}].

Then, for each case in the 5000 combinations, we randomly selected six combinations of solar zenith angles θ_0, viewing zenith angles θ, and relative azimuth angles $\Delta\phi$, which were allowed to vary in the following ranges:

1. θ_0: 0–80 [°],
2. θ: 0–70 [°],
3. $\Delta\phi$: 0–180 [°].

In addition to the randomly varied sun-sensor geometries, the radiance in the nadir direction, i.e., $\theta = 0°$, was always computed and from it the remote sensing reflectance for each case was derived. The solar irradiance just above the ocean surface (E_d^{0+}) was also computed for each case. Then we computed the remote sensing reflectance for every sun-sensor geometry in each case:

$$R_{\text{rs}}(\theta_0, \theta, \Delta\phi) = \frac{L_w(0^+, \theta_0, \theta, \Delta\phi)}{E_d(0^+)}, \tag{23}$$

where $L_w(0^+, \theta_0, \theta, \Delta\phi)$ is given by Eq. (5). The remote sensing reflectances were rearranged into two groups. One group included all the angle-dependent remote sensing reflectances $R_{\text{rs}}(\lambda_i, \theta_0, \theta, \Delta\phi)$, while the other group included the spectrum of the corresponding nadir remote sensing reflectances, $R_{\text{rs}}(\lambda_i, \theta_0)$. We then created a neural network with two hidden layers. The first layer uses RBFs [11] as neurons and the second layer uses linear function as neurons. The number of neurons is the same in both layers and can be adjusted to meet the required accuracy. The input to our neural network training is the three geometry angles plus the angle-dependent remote sensing reflectances, $[\theta_0, \theta, \Delta\phi, R_{\text{rs}}(\lambda_i, \theta_0, \theta, \Delta\phi)]$, and the output is the second group of the remote sensing reflectance data, $R_{\text{rs}}(\lambda_i, \theta_0)$, for each case and sun-sensor geometry configuration. After the training, the nadir remote sensing reflectance can be derived from a single equation:

$$R_{\text{rs}}(\lambda_i, \theta_0) = \sum_{j=1}^{N} a_{ij} \exp\left[-b^2 \sum_{k=1}^{N_{\text{in}}} (p_k - c_{jk})^2\right] + d_i, \tag{24}$$

where N is the number of neurons, b and c_{jk} are the bias and weight in the first layer, and a_{ij} and d_i are the weight and bias in the second layer. These weights and biases are optimized from the training procedure to minimize the error between the neural-network-derived $R_{\text{rs}}(\lambda_i, \theta_0)$ and the actual $R_{\text{rs}}(\lambda_i, \theta_0)$ values in the training dataset. N_{in} is the number of input parameters, which in our neural network equals 10:3 geometry angles plus seven wavelengths. p_k denotes the input parameters, which in our case are the three geometry angles and the angle-dependent remote sensing reflectances at each wavelength.

The training procedure iteratively creates the neural network one RBF neuron at a time. The training starts by computing an average value of the actual $R_{\text{rs}}(\lambda_i, \theta_0)$ over the 30,000 training cases. The case that has the largest deviation from the average value was picked, and the input of this case was used to create the first RBF neuron, i.e., setting $c_{1k} = p_k$. The bias b was set to 0.8326 for all RBF neurons. Then b and c_{1k} were put into Eq. (24) to solve for a_{i1} and d_i and a network with one RBF neuron was created. Then this one neuron network was used to compute $R_{\text{rs}}(\lambda_i, \theta_0)$, the error between neural network simulated $R_{\text{rs}}(\lambda_i, \theta_0)$, and the actual $R_{\text{rs}}(\lambda_i, \theta_0)$ was computed for all input cases. The case with the largest error was used to create the next RBF neuron. Then the two RBF neurons were inserted into Eq. (24) to solve for a_{ij} and d_i and a network with two RBF neurons was created. This procedure was repeated iteratively until the error between the neural network derived $R_{\text{rs}}(\lambda_i, \theta_0)$ and the actual $R_{\text{rs}}(\lambda_i, \theta_0)$ value reached a preset tolerance or the maximum number of neurons was reached. In our study, we used 500 neurons in both layers.

3. VALIDATION OF THE NEURAL NETWORK METHOD

A. Synthetic Data Analysis

We first tested our neural network algorithm with a synthetic validation dataset. For this purpose we used the CCRR simulation dataset [23], which is similar to the synthetic dataset documented in IOCCG Report5 [35]. In this dataset, there are 5000 combinations of the three ocean parameters, CHL, MIN, and CDOM, paired with 5000 simulated normalized remote sensing reflectances generated by the Hydrolight v5.0 RTM. The 5000 combinations of the ocean parameters are

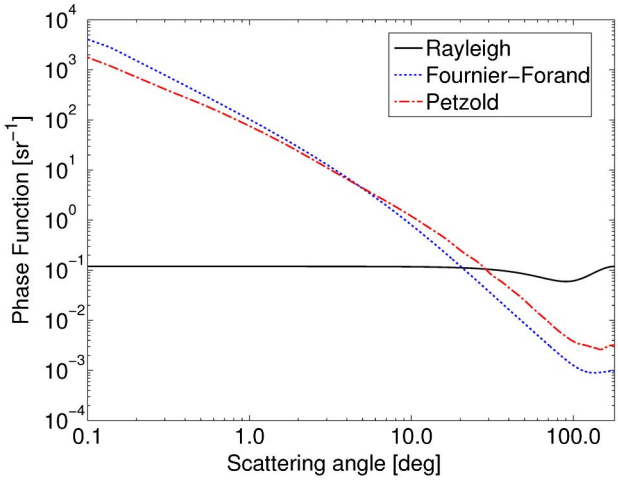

Fig. 3. Fournier–Forand (FF), Petzold, and Rayleigh phase functions used in this paper.

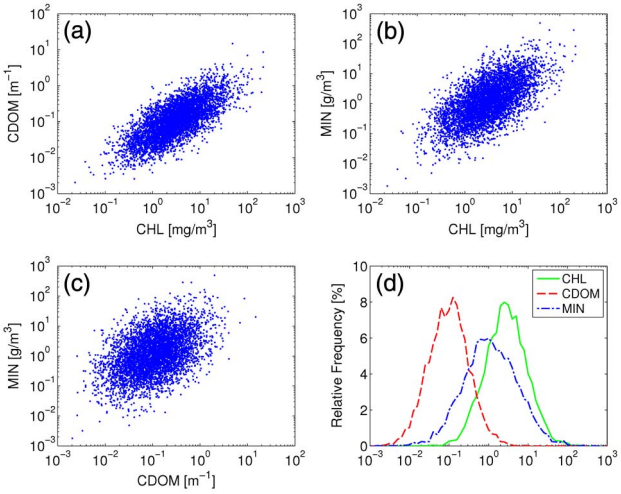

Fig. 4. Covariation and distribution of CHL, MIN, and CDOM in the CCRR synthetic dataset. Panels (a), (b), and (c) show the covariation between CHL and CDOM, CHL and MIN, and CDOM and MIN, respectively. Panel (d) shows the distribution of CHL (green solid line), MIN (blue dashed-dotted line), and CDOM (red dashed line). The units of CHL, MIN, and CDOM are the same as in the first three panels.

sampled in such a manner that the covariation between any two parameters matches that obtained from field measurements in coastal waters around Europe [29]. Figure 4 shows the covariation (panels a, b, and c) and distribution (panel d) of the three ocean parameters in this synthetic dataset.

We did a comparison between the $R_{rs}(\lambda_i, \theta_0)$ in the CCRR simulation dataset and $R_{rs}(\lambda_i)$ values generated by AccuRT, using the ocean parameters from the CCRR simulation dataset. The match was very close, and the correlation between the two datasets has an R^2 value no less than 0.999 for all the wavelengths [36]. This good match means that AccuRT produces output very close to that of Hydrolight. We then used the 5000 cases of CHL, MIN, and CDOM to generate a validation dataset in the same way as we generated the training dataset. The three aerosol parameters, $\tau_a(865)$, f_a, and RH, were still randomly selected in the same range as described in Section 2.C. The values of CHL, MIN, and CDOM are from the 5000 simulation cases and, for each of the 5000 cases, we randomly selected one solar zenith angle θ_0, four viewing zenith angles θ, and four relative azimuth angles $\Delta\phi$ in the same range as in Section 2.C., resulting in 80,000 cases for different sun-sensor geometries, water, and atmospheric IOPs. The 80,000 cases were input into AccuRT to compute angle-dependent remote sensing reflectances $R_{rs}(\lambda_i, \theta_0, \theta, \Delta\phi)$ as well as the corresponding nadir remote sensing reflectances $R_{rs}(\lambda_i, \theta_0)$.

The 80,000 validation data points were also divided into two groups, one group including the angle-dependent remote sensing reflectances $R_{rs}(\lambda_i, \theta_0, \theta, \Delta\phi)$ and the other group including the nadir remote sensing reflectances $R_{rs}(\lambda_i, \theta_0)$. These data were first used to do a statistical analysis of the differences between the two groups, which shows the anisotropy of the remote sensing reflectance. The results are shown in Fig. 5. The first panel shows the distribution of the difference between remote sensing reflectances $R_{rs}(\lambda_i, \theta_0, \theta, \Delta\phi)$ and nadir remote sensing reflectances $R_{rs}(\lambda_i, \theta_0)$ at 443 nm for all the 80,000 cases. The second panel shows the difference for two different types of water. The green line represents clean or Case 1 water and the red line represents moderate/turbid or Case 2 water. The third panel shows how the anisotropy depends on the sun-sensor geometry: the black line shows the variation with solar zenith angle θ_0, the red line shows the variation with viewing zenith angle θ, and the blue line shows the variation with relative azimuth angle $\Delta\phi$. For other wavelengths, similar results were found, so here we just show one of them as an example. This statistical analysis indicates that the remote sensing reflectance is far from isotropic. For clean water, the average difference between angle-dependent remote sensing

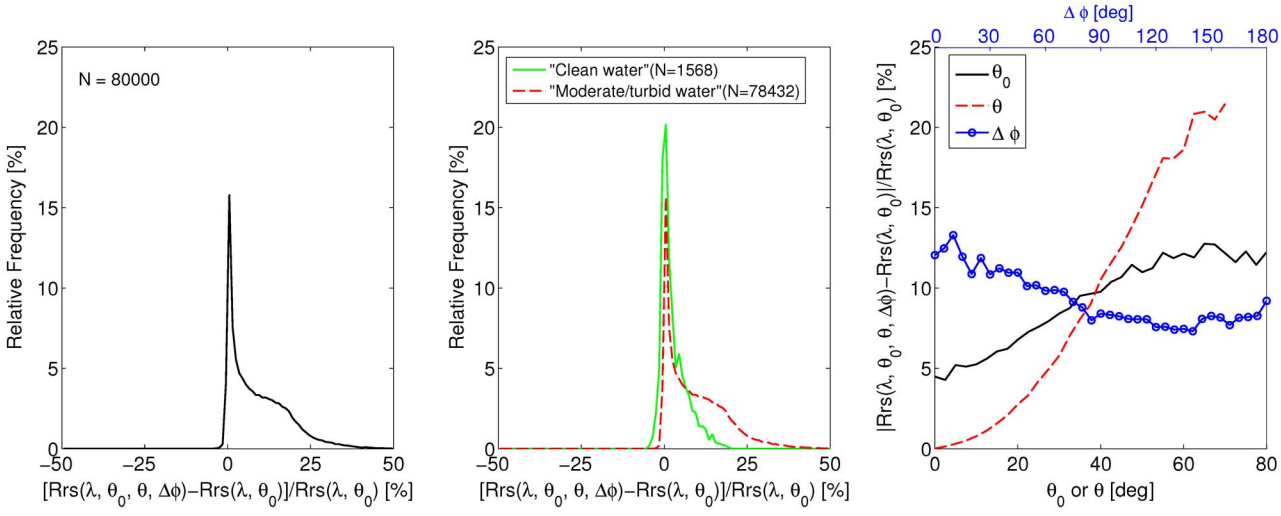

Fig. 5. Statistics of the percentage difference between the viewing angle-dependent $R_{rs}(\lambda_i, \theta_0, \theta, \Delta\phi)$ and the nadir $R_{rs}(\lambda_i, \theta_0)$ for 80,000 simulation data. Panel 1 shows the distribution of the difference for all cases, panel 2 shows the distribution of the difference for "clean" (CHL < 0.5[mg/m^3], CDOM < 0.2[m^{-1}], MIN < 0.1[g/m^3]) and "moderate/turbid" (the rest of the data) waters, and panel 3 shows the dependence on the sun-sensor geometry.

reflectances and corresponding nadir remote sensing reflectances is 2.77%–5.09% for different wavelengths and the maximum is around 25%. For moderate/turbid water, the average difference increases to 8.74%–9.95%, with a maximum around 56%. The anisotropy of the remote sensing reflectance has a weak dependence on solar zenith angle and relative azimuth angle, but depends strongly on viewing zenith angle.

We then applied our neural network algorithm to derive nadir $R_{rs}(\lambda_i, \theta_0)$ from the viewing-angle-dependent $R_{rs}(\lambda_i, \theta_0, \theta, \Delta\phi)$ for the 80,000 validation data and compared the neural-network-derived nadir remote sensing reflectance $R_{rs}^{NN}(\lambda_i)$ with the AccuRT-generated remote sensing reflectance $R_{rs}^{Mod}(\lambda_i)$. For comparison, we also applied the MAG02 algorithm to our validation dataset. The MAG02 algorithm requires CHL as input. However, in satellite remote sensing, CHL is usually derived from maximum band ratio algorithm (OC4) or the IOP model. To show the performance of the MAG02 algorithm in the application to satellite remote sensing, we applied the Ocean Color Chlorophyll-*a* Algorithm OC4 v6 [37] to estimate the CHL from the angle-dependent remote sensing reflectance $R_{rs}(, \lambda_i, \theta_0, \theta, \Delta\phi)$ instead of using the actual CHL that was used to generate the validation dataset. Then the three geometry angles and the estimated CHL were input into the MAG02 algorithm to evaluate the correction factor that is used to derive nadir $R_{rs}(\lambda_i, \theta_0)$ values from the corresponding $R_{rs}(\lambda_i, \theta_0, \theta, \Delta\phi)$ values. The nadir remote sensing reflectance derived from the MAG02 algorithm [denoted $R_{rs}^{MAG}(\lambda_i, \theta_0)$] was also compared with the AccuRT-generated remote sensing reflectance $R_{rs}^{Mod}(\lambda_i, \theta_0)$. To quantify the performance of the algorithms, we computed the coefficient of determination (R^2), percentage error (PE), and bias between algorithm-derived and AccuRT-generated remote sensing reflectances. The coefficient of determination is given by:

$$R^2 = \frac{\left[\frac{1}{N}\sum(X - \bar{X})(Y - \bar{Y})\right]^2}{\sigma_X^2 \sigma_Y^2}, \tag{25}$$

where $X = R_{rs}^{NN/MAG}(\lambda_i)$, $Y = R_{rs}^{Mod}(\lambda_i)$, and σ is the standard deviation. The percentage error is

$$\mathrm{PE}[\%] = \left| \frac{R_{rs}^{NN/MAG}(\lambda_i) - R_{rs}^{Mod}(\lambda_i)}{R_{rs}^{Mod}(\lambda_i)} \right| \times 100. \tag{26}$$

and the bias is

$$\mathrm{bias}[\%] = \frac{R_{rs}^{NN/MAG}(\lambda_i) - R_{rs}^{Mod}(\lambda_i)}{R_{rs}^{Mod}(\lambda_i)} \times 100. \tag{27}$$

Figure 6 shows the percentage error distribution in remote sensing reflectances derived from the two algorithms. It is

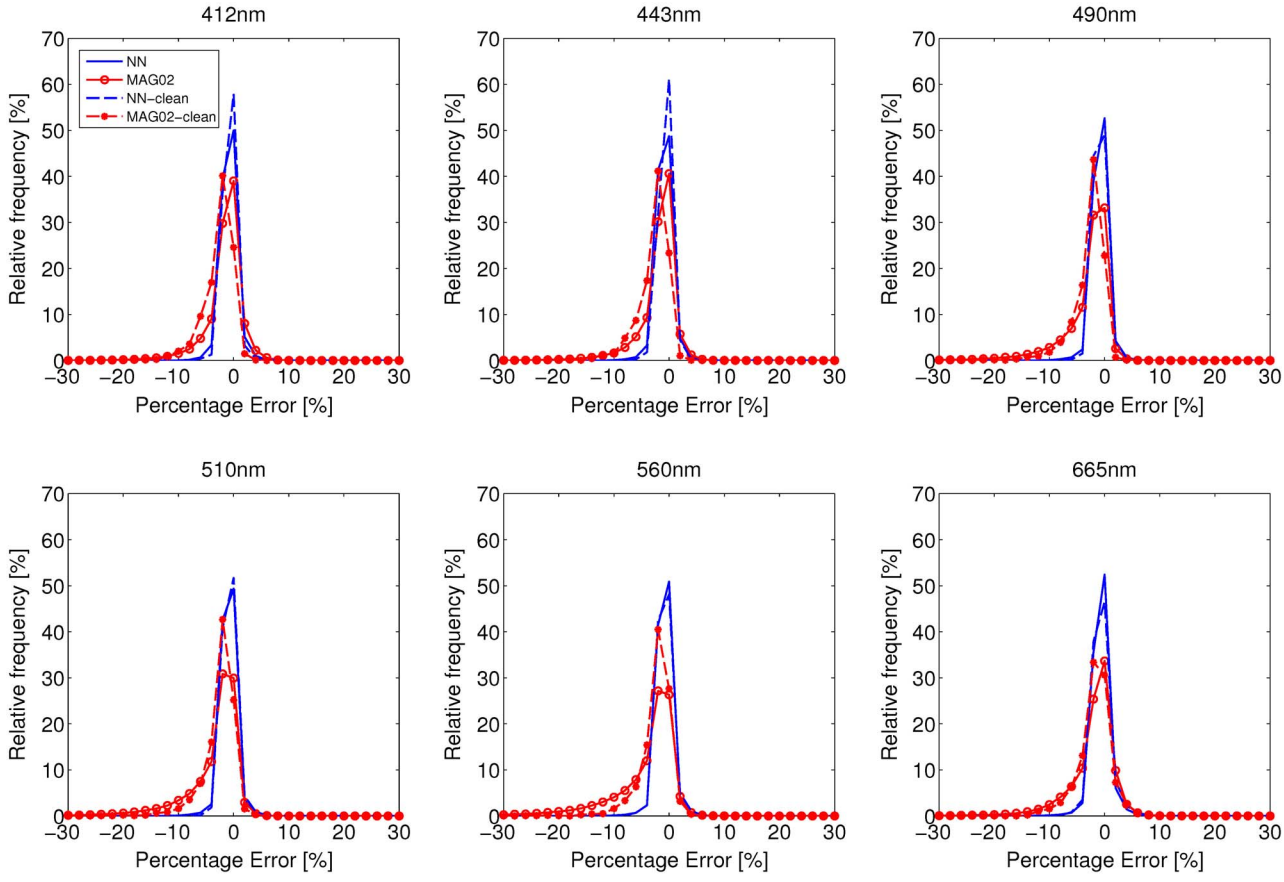

Fig. 6. Distributions of the percentage error between R_{rs}^{NN} and R_{rs}^{Mod}, and between R_{rs}^{MAG} and R_{rs}^{Mod} for the validation data at six wavelengths: 412, 443, 490, 510, 560, and 665 nm. The blue solid line is the percentage error distribution of R_{rs}^{NN} for all 80,000 validation data, the blue dashed line is the percentage error distribution of R_{rs}^{NN} for "clean" water cases, the red solid line with circles is the percentage error distribution of R_{rs}^{MAG} for all 80,000 validation data, and the red dashed line with stars is the percentage error distribution of R_{rs}^{MAG} for Case 1 water cases.

Table 1. Coefficient of Determination (R^2) of Derived Nadir R_{rs}[a]

	All Cases ($N = 80{,}000$)			Clean ($N = 1568$)			Moderate/Turbid ($N = 78{,}432$)			$\theta > 60°$ ($N = 9884$)		
λ [nm]	No BRDF	MAG02	NN	No BRDF	MAG02	NN	No BRDF	MAG02	NN	No BRDF	MAG02	NN
412	0.9820	0.9975	0.9996	0.9950	0.9970	0.9979	0.9821	0.9975	0.9996	0.9900	0.9935	0.9990
443	0.9803	0.9961	0.9995	0.9925	0.9962	0.9992	0.9803	0.9961	0.9995	0.9902	0.9902	0.9987
490	0.9805	0.9904	0.9995	0.9879	0.9944	0.9992	0.9803	0.9903	0.9995	0.9878	0.9800	0.9987
510	0.9818	0.9877	0.9996	0.9866	0.9942	0.9991	0.9815	0.9875	0.9996	0.9870	0.9754	0.9988
560	0.9855	0.9819	0.9997	0.9849	0.9938	0.9988	0.9853	0.9816	0.9997	0.9864	0.9662	0.9991
620	0.9896	0.9872	0.9998	0.9836	0.9953	0.9984	0.9895	0.9872	0.9998	0.9881	0.9739	0.9995
665	0.9901	0.9900	0.9998	0.9785	0.9916	0.9982	0.9900	0.9900	0.9998	0.9877	0.9786	0.9995

[a]From the synthetic dataset using the isotropic assumption, i.e., no BRDF correction, the MAG02 algorithm, and our NN algorithm results are shown at all wavelengths for all synthetic data, "clear" water synthetic data, "moderate/turbid" water synthetic data, and data with large viewing angles.

Table 2. Mean Absolute PE [%] of Derived Nadir R_{rs}[a]

	All Cases ($N = 80{,}000$)			Clean ($N = 1568$)			Moderate/Turbid ($N = 78{,}432$)			$\theta > 60°$ ($N = 9884$)		
λ [nm]	No BRDF	MAG02	NN	No BRDF	MAG02	NN	No BRDF	MAG02	NN	No BRDF	MAG02	NN
412	8.62	2.00	0.80	2.77	2.04	0.73	8.74	2.00	0.80	19.07	2.51	1.53
443	9.26	2.02	0.78	3.15	2.06	0.72	9.38	2.02	0.78	20.31	2.81	1.53
490	9.83	2.73	0.72	4.05	2.06	0.68	9.93	2.74	0.72	21.07	4.10	1.52
510	9.85	3.14	0.71	4.14	1.93	0.69	9.95	3.16	0.70	20.96	4.59	1.48
560	9.70	3.99	0.69	4.44	1.87	0.78	9.80	4.03	0.69	20.31	5.49	1.45
620	9.72	2.91	0.84	4.58	1.94	1.02	9.81	2.93	0.83	20.95	3.83	1.68
665	9.60	2.68	0.94	5.09	2.23	1.11	9.68	2.69	0.93	20.70	3.25	1.96

[a]From the synthetic dataset using the isotropic assumption, i.e., no BRDF correction, the MAG02 algorithm, and our NN algorithm results are shown at all wavelengths for all synthetic data, "clear" water synthetic data, "moderate/turbid" water synthetic data, and data with large viewing angles.

Table 3. Mean Bias [%] in Derived Nadir R_{rs}[a]

	All Cases ($N = 80{,}000$)			Clean ($N = 1568$)			Moderate/Turbid ($N = 78{,}432$)			$\theta > 60°$ ($N = 9884$)		
λ [nm]	No BRDF	MAG02	NN	No BRDF	MAG02	NN	No BRDF	MAG02	NN	No BRDF	MAG02	NN
412	8.57	−0.71	0.11	2.25	−1.71	0.26	8.69	−0.70	0.11	19.04	−1.86	0.32
443	9.22	−1.04	0.05	2.73	−1.80	0.28	9.35	−1.02	0.05	20.27	−2.31	0.26
490	9.80	−2.20	0.11	3.77	−1.82	0.18	9.92	−2.21	0.11	21.05	−3.70	0.43
510	9.82	−2.59	0.04	3.74	−1.56	0.17	9.94	−2.61	0.04	20.92	−4.11	0.31
560	9.67	−3.33	0.06	3.88	−1.37	0.14	9.78	−3.37	0.05	20.26	−4.78	0.29
620	9.55	−1.75	0.17	3.10	−0.91	0.10	9.68	−1.76	0.17	20.73	−2.58	0.50
665	9.31	−1.24	0.24	3.31	−0.78	0.25	9.43	−1.25	0.24	20.38	−1.65	0.77

[a]From the synthetic dataset using the isotropic assumption, i.e., no BRDF correction, the MAG02 algorithm, and our NN algorithm results are shown at all wavelengths for all synthetic data, "clear" water synthetic data, "moderate/turbid" water synthetic data, and data with large viewing angles.

quite noticeable that our NN algorithm outperforms the MAG02 algorithm. The solid lines show a comparison using the entire 80,000 validation dataset. The percentage error in our NN algorithm is generally less than 5%, and the mean absolute percentage error is 0.69%–0.94% for all wavelengths. The MAG02 algorithm generally underestimated the remote sensing reflectance, and the mean absolute percentage error is 2.00%–3.99%. Considering that the MAG02 algorithm was designed for Case 1 water, we applied a filter (CHL $< 0.5[\mathrm{mg/m^3}]$, CDOM $< 0.2[\mathrm{m^{-1}}]$, MIN $< 0.1[\mathrm{g/m^3}]$) to the validation dataset to select clean water cases and we found 1,568 qualified data points. However, we need to point out that the filter we applied

should not be used as the criteria for the classification of Case 1 and Case 2 water. The filter returns clean water cases with relatively little influence from CDOM and mineral particles, and these cases can be considered to be close to Case 1 water. The same comparison is shown in Fig. 6 as dashed lines. For clean Case 1 water, our NN algorithm still performs well, with a mean absolute percentage error of 0.68%–1.11%. The MAG02 algorithm performs best at green and red wavelengths, with a mean absolute percentage error of 1.87%–2.23%. Detailed comparisons of the coefficient of determination (R^2), PE, and bias for all wavelengths are shown in Tables 1–3. In the detailed comparison, we also added the results obtained by using the isotropic assumption, i.e., no BRDF correction, which compares $R_{rs}(\lambda_i, \theta_0)$ with $R_{rs}(\lambda_i, \theta_0, \theta, \Delta\phi)$ directly. In each table, we show the comparison in four different ways: all 80,000 cases, clean water cases, moderate/turbid water cases, and large viewing zenith angle cases. The comparison shows that our NN algorithm works well in both clean and turbid waters. The performance is stable and the error is generally less than 1.2%. For large viewing zenith angles, the error slightly increases but is still within 2%. The MAG02 algorithm, on the other hand, performs well in clean Case 1 waters but is slightly worse in turbid waters. The error increases to a maximum value of 4.03%. For large viewing zenith angles, the MAG02 algorithm also shows improvement over the isotropic treatment, with an error no larger than 5.5%.

B. NuRADS Field Measurement Data

NuRADS [38] is a compact camera system that takes images of the upward radiance just below the ocean surface at various geometry angles and multiple wavelengths centered at 411, 436, 487, 526, 548, and 616 nm. This instrument has been used in many experiments and a large quantity of *in situ* data is available in the NASA SeaBASS validation data base. The NuRADS measurements provide the upward radiance in the nadir direction, $L_u^{\mathrm{NuR}}(\lambda_i, \theta_0)$, and the below surface bidirectional effect (BDE), defined as

$$\mathrm{BDE}_{\mathrm{NuR}} = L_u^{\mathrm{NuR}}(\theta_0, \theta', \Delta\phi, \lambda_i)/L_u^{\mathrm{NuR}}(\lambda_i, \theta_0), \quad (28)$$

where $L_u^{\mathrm{NuR}}(\theta_0, \theta', \Delta\phi, \lambda_i)$ are the measured upward radiances at non-nadir geometry angles. Here we used the notation BDE instead of BRDF to avoid confusion because the ratio was computed using the underwater radiance instead of the remote sensing reflectance (R_{rs}) in Eq. (28). In the SeaBASS database, the BDE data are given in every 5° for viewing angles in the range of 0°–70° and every 10° for relative azimuth angles in the range of 0°–180°. The solar zenith angles are also given for each NuRADS measurement. In our validation test, we selected data that have viewing zenith angles in the range of 0°–45° and relative azimuth angles in the range of 0°–180°. Therefore, in each measurement, there are 171 (9 viewing zenith angles ×19 relative azimuth angles) BDE data points for different geometry angles.

We selected data from four experiments—BP09, SORTIE2, BIOSOPE, and Ocean Color Calibration & Validation (OCCV)—as our field measurement validation dataset. The locations where the four experiments were conducted are shown in Fig. 7. These four experiments have field measurements of CHL, which are required as input in the MAG02 algorithm. Three filters were applied in the data selection:

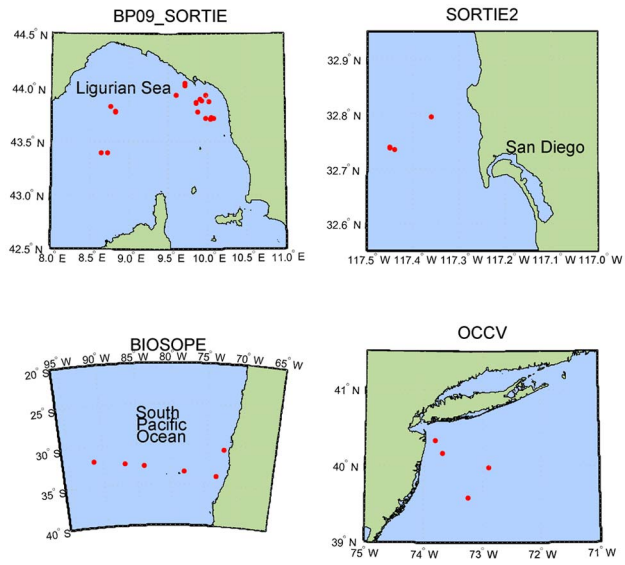

Fig. 7. Locations of the four experiments selected for validation.

(i) we excluded the data from the 616 nm channel due to instrument self-shading. (ii) Some of the measurements do not have data available at all NuRADS wavelengths (excluding 616 nm) due to the measurement procedure and data quality, but our NN algorithm requires the entire spectrum as input. Therefore, only measurements that had the entire spectrum of data available were selected. (iii) The measurements of CHL do not match the NuRADS measurements in time exactly, so we only selected the NuRADS measurements that have measured CHL values available within ±3 h. After we apply these filters, there are 28 measurements from the BP09 experiment, 13 from the SORTIE2 experiment, 11 from the BIOSOPE experiment, and 7 from OCCV experiment among the data selected.

There were no measurements of downward irradiance, E_d, available in the dataset, so the remote sensing reflectance cannot be derived directly from the L_u data. We modified our NN algorithm to train a new neural network that computes the upward radiance directly instead of computing $R_{rs}(\lambda_i, \theta_0, \theta, \Delta\phi)$. We first generated a training dataset using AccuRT in the same way as described in Section 2.C. at the NuRADS wavelengths, but instead of outputting upward radiances above the ocean surface and computing $R_{rs}(\theta_0, \theta, \Delta\phi)$ [see Eq. (23)], we output the upward radiances just below the surface and used them directly to train the neural network. Hence, the two groups in the training dataset are $L_u(\lambda_i, \theta_0, \theta', \Delta\phi)/\cos(\theta_0)$ and $L_u(\lambda_i, \theta_0)/\cos(\theta_0)$, and the neural network was trained to compute the nadir radiance, $L_u(\lambda_i, \theta_0)$, from the viewing angle-dependent upward radiance, $L_u(\lambda_i, \theta_0, \theta', \Delta\phi)$. The viewing angle-dependent upward radiance was obtained directly from the NuRADS measurements using Eq. (28), and our NN algorithm computes the nadir radiance $L_u^{\mathrm{NN}}(\lambda_i, \theta_0)$ from the angle-dependent radiances. Then we computed the BDE derived by our NN algorithm as

$$\mathrm{BDE}_{\mathrm{NN}} = L_u^{\mathrm{NN}}(\theta_0, \theta', \Delta\phi, \lambda_i)/L_u^{\mathrm{NN}}(\lambda_i, \theta_0). \quad (29)$$

The BDE derived from the NN algorithm was then compared with the NuRADS-measured BDE to quantify the errors.

The MAG02 algorithm requires the geometry angles and the CHL as input, and we only used the measured CHL at the surface level. The CHL value and the geometry angles are then used in the MAG02 algorithm to compute the f/Q factor, and the BDE was determined from [6]

$$\mathrm{BDE}_{\mathrm{MAG02}} = \frac{f(\theta_0, \theta', \Delta\phi, \lambda_i)/Q(\theta_0, \theta', \Delta\phi, \lambda_i)}{f(\theta_0, 0, 0, \lambda_i)/Q(\theta_0, 0, 0, \lambda_i)}. \quad (30)$$

The BDE derived from the MAG02 algorithm was also compared with the NuRADS-measured BDE to quantify the errors.

A comparison of the percentage error distributions of the BDE values derived by the NN algorithm and the MAG02 algorithm is shown in Fig. 8 and more detailed comparisons of the coefficient of determination (R^2), PE, and bias are provided in Tables 4–6. We note that our NN algorithm works best in the SORTIE2 experiment. This experiment was conducted in January 2008 near San Diego Bay, where the water is generally Case 2 with not only high chlorophyll concentrations (>4 mg/m^3) but also high sediment particle loading brought by the San Diego river and suspended around the shore area. The NN algorithm works well in this area perhaps due to our use of the Petzold phase function which was derived from data measured there, although more than 40 years ago. The MAG02 algorithm does not work well for the SORTIE2 experiment as expected, since the algorithm was developed for Case 1 waters.

The BP09 experiment was conducted in the Ligurian Sea in March 13–26, 2009. The water in this area can be classified as Case 2, since nonalgal particles are present in the water and the concentration of total suspended matter is in the range 0.25 – 1.20 g/m^3 with an average of about 0.55 g/m^3 during the experiment. However, there was a Spring algal bloom in the area during the experiment, so the water was generally dominated by algal particles. The CHL was in the range 0.26 – 4.37 mg/m^3 with an average value of about 1.17 mg/m^3. We found that our NN algorithm and the MAG02 algorithm worked equally well for this type of water.

The BIOSOPE experiment was conducted in the south Pacific Ocean in October–December, 2004. The measurements we selected from this experiment are generally Case 1 water and the chlorophyll concentration is less than 0.3 mg/m^3 for the offshore measurements and no more than 1.4 mg/m^3 for the near-shore measurements. We found our NN algorithm to perform very similar to the MAG02

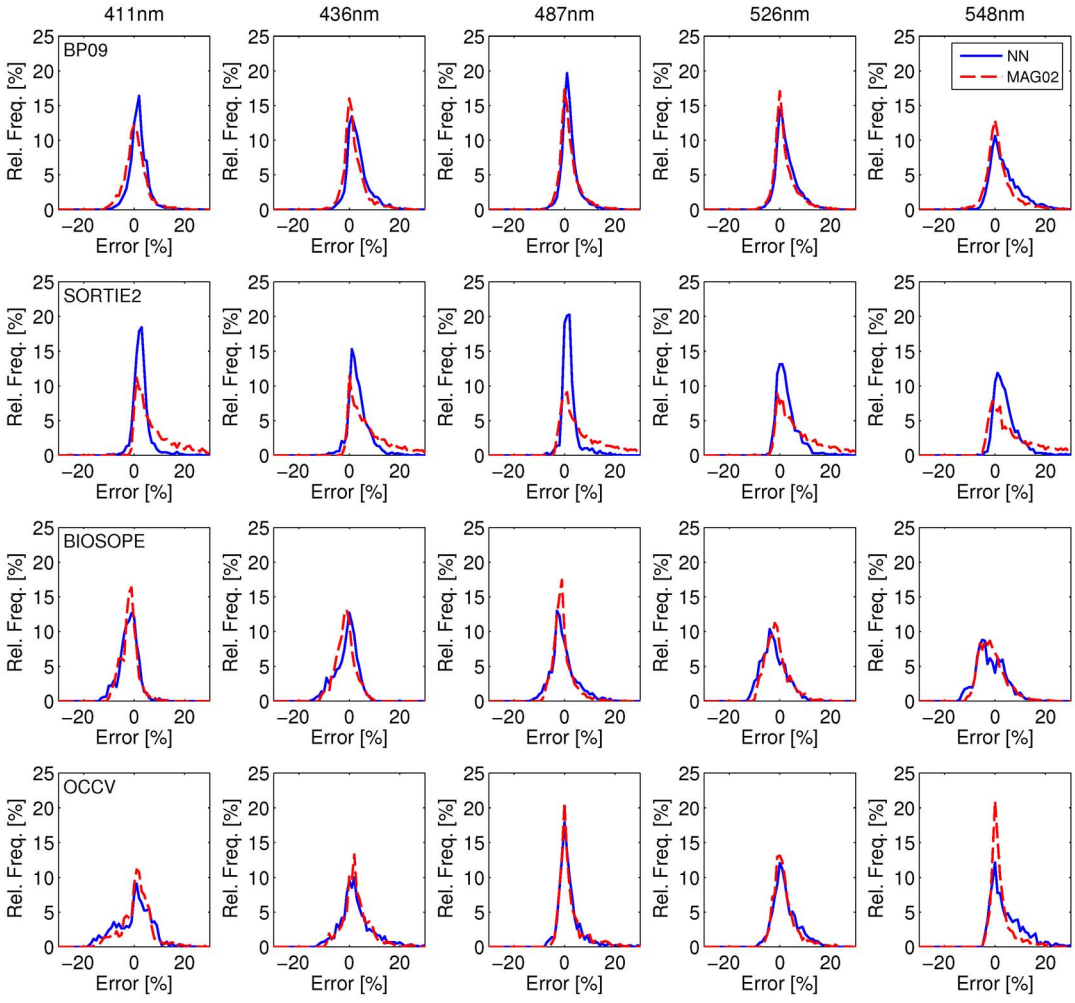

Fig. 8. Comparison of the percentage error distribution of the BDE derived from NN algorithm (blue) and MAG02 algorithm (red). From top to bottom, each row shows the comparison for experiments BP09, SORTIE2, BIOSOPE, and OCCV, respectively, and from left to right, the columns are 411, 436, 487, 526, and 548 nm, respectively.

Table 4. Coefficient of Determination (R^2) of BDE Values[a]

	BP09 ($N = 4788$)		SORTIE2 ($N = 2223$)		BIOSOPE ($N = 1881$)		OCCV ($N = 1197$)	
λ [nm]	NN	MAG02	NN	MAG02	NN	MAG02	NN	MAG02
411	0.872	0.747	0.798	0.528	0.742	0.726	0.700	0.748
436	0.864	0.776	0.803	0.642	0.749	0.688	0.626	0.742
487	0.912	0.872	0.888	0.716	0.686	0.729	0.816	0.876
526	0.888	0.837	0.885	0.863	0.590	0.516	0.822	0.841
548	0.891	0.816	0.894	0.828	0.576	0.459	0.852	0.859

[a]Derived from NuRADS measurements using the NN and MAG02 algorithms. Results are shown at all wavelengths for the four validation datasets: BP09, SORTIE, BIOSOPE, and OCCV.

Table 5. Mean Absolute PE [%] of BDE Values[a]

	BP09 ($N = 4788$)		SORTIE2 ($N = 2223$)		BIOSOPE ($N = 1881$)		OCCV ($N = 1197$)	
λ [nm]	NN	MAG02	NN	MAG02	NN	MAG02	NN	MAG02
411	3.208	3.344	3.742	9.131	2.998	2.700	5.581	4.668
436	4.255	3.362	4.473	9.459	3.319	2.978	5.587	4.886
487	2.996	3.214	2.806	9.757	3.727	2.790	3.392	3.470
526	3.750	3.514	3.732	9.787	4.217	3.639	4.067	3.415
548	5.275	4.994	4.896	10.511	4.685	4.132	5.630	3.218

[a]Derived from NuRADS measurements using the NN and MAG02 algorithms. Results are shown at all wavelengths for the four validation datasets: BP09, SORTIE, BIOSOPE, and OCCV.

Table 6. Mean Bias [%] of BDE Values[a]

	BP09 ($N = 4788$)		SORTIE2 ($N = 2223$)		BIOSOPE ($N = 1881$)		OCCV ($N = 1197$)	
λ [nm]	NN	MAG02	NN	MAG02	NN	MAG02	NN	MAG02
411	2.291	1.149	3.368	9.035	−1.621	−1.395	0.475	1.611
436	3.844	2.386	4.026	9.388	−0.754	−0.984	2.924	3.463
487	2.472	2.461	2.458	9.390	0.068	−0.303	2.432	2.737
526	3.117	2.571	3.281	9.496	−1.889	−0.720	2.785	2.251
548	4.499	3.183	4.697	9.831	−1.243	−0.636	4.907	2.691

[a]Derived from NuRADS measurements using the NN and MAG02 algorithms. Results are shown at all wavelengths for the four validation datasets: BP09, SORTIE, BIOSOPE, and OCCV.

algorithm in this Case 1 water; our NN algorithm performs better in terms of R^2 correlation with the *in situ* measured data whereas the MAG02 algorithm has slightly smaller mean absolute percentage error.

The OCCV experiment was conducted in the New Jersey Bight in May, 2009. The water in this area is also chlorophyll-dominated. The offshore measurements had chlorophyll concentrations of 0.2 mg/m^3, while the near-shore measurements had chlorophyll concentration of 7.85 mg/m^3. The Hudson river brings sediment particles to the water in this area, but in May the concentration of total suspended matter in the surface water of the lower bay area is generally less than 2 g/m^3. A comparison of BDE values derived by our NN algorithm and the MAG02 algorithm shows similar results also in this area. The MAG02 algorithm slightly outperforms our NN algorithm because the water is dominated by algal particles.

4. CONCLUSIONS

The remote sensing reflectance of oceanic water is generally anisotropic and this anisotropy must be corrected for in remote sensing applications that make use of the nadir water-leaving radiance to derive ocean color products. The correction to nadir of the water-leaving radiance is also important when comparing and merging products from different satellite missions. The standard correction method developed by Morel *et al.* [6], based on the Case 1 assumption, is unsuitable for Case 2 waters such as rivers, lakes, and coastal waters. The standard method requires the chlorophyll concentration as an input, and such a requirement cannot easily be fulfilled in remote sensing applications because the chlorophyll concentration is generally produced from the corrected remote sensing reflectance.

To meet the need for a correction method that works for waters that may be turbidity- and/or CDOM-dominated, we developed an algorithm that directly converts the remote sensing reflectance from the slant to the nadir viewing direction using a neural network approach. The neural network was trained using remote sensing reflectances at slant and nadir directions. The remote sensing reflectance was generated from a RTM in which scattering phase functions for algal and nonalgal particles were adopted. Therefore the remote sensing reflectance implicitly contains information about the shape of the phase function which affects the BRDF. This method uses

spectral remote sensing reflectances as input; hence, it does not require any prior knowledge of the water constituents or their optical properties. Tests based on synthetic data show that this method is sound and accurate. Validation using NuRADS measurements [38] shows that our neural network method works equally well compared to the standard method for Case 1 or chlorophyll-dominated waters. For Case 2 waters, a significant improvement over the standard method was found, especially for waters dominated by sediment particles.

Funding. National Aeronautics and Space Administration (NASA).

REFERENCES

1. H. R. Gordon and D. K. Clark, "Clear water radiances for atmospheric correction of coastal zone color scanner imagery," Appl. Opt. **20**, 4175–4180 (1981).
2. A. Morel and B. Gentili, "Diffuse reflectance of oceanic waters: its dependence on sun angle as influenced by the molecular scattering contribution," Appl. Opt. **30**, 4427–4438 (1991).
3. A. Morel and B. Gentili, "Diffuse reflectance of oceanic waters II: bidirectional aspects," Appl. Opt. **32**, 6864–6879 (1993).
4. A. Morel and B. Gentili, "Diffuse reflectance of oceanic waters III: implication of bidirectionality for the remote-sensing problem," Appl. Opt. **35**, 4850–4862 (1996).
5. C. Cox and W. Munk, "Measurement of the roughness of the sea surface from photographs of the sun's glitter," J. Opt. Soc. Am. **44**, 838–850 (1954).
6. A. Morel, D. Antoine, and B. Gentili, "Bidirectional reflectance of oceanic waters: accounting for Raman emission and varying particle scattering phase function," Appl. Opt. **41**, 6289–6306 (2002).
7. K. J. Voss, A. Morel, and D. Antoine, "Detailed validation of the bidirectional effect in various Case 1 waters for application to ocean color imagery," Biogeosciences **4**, 781–789 (2007).
8. A. C. R. Gleason, K. J. Voss, H. R. Gordon, M. Twardowski, J. Sullivan, C. Trees, A. Weidemann, J. F. Berthon, D. Clark, and Z. P. Lee, "Detailed validation of the bidirectional effect in various case I and case II waters," Opt. Express **20**, 7630–7645 (2012).
9. Z. P. Lee, K. Du, K. J. Voss, G. Zibordi, B. Lubac, R. Arnone, and A. Weidemann, "An inherent-optical property-centered approach to correct the angular effects in water-leaving radiance," Appl. Opt. **50**, 3155–3167 (2011).
10. A. Gilerson, S. Hlaing, T. Harmel, A. Tonizzo, R. Arnone, A. Weidemann, and S. Ahmed, "Bidirectional reflectance function in coastal waters: modeling and validation," Proc. SPIE **8175**, 81750O (2011).
11. D. S. Broomhead and D. Lowe, "Radial basis functions, multi-variable functional interpolation and adaptive networks," Complex Syst. **2**, 321–355 (1988).
12. Z. Jin and K. Stamnes, "Radiative transfer in nonuniformly refracting media such as the atmosphere/ocean system," Appl. Opt. **33**, 431–442 (1994).
13. G. E. Thomas and K. Stamnes, *Radiative Transfer in the Atmosphere and Ocean*, 2nd ed. (Cambridge University, 2002).
14. B. Hamre, S. Stamnes, K. Stamnes, and J. J. Stamnes, "C-DISORT: a versatile tool for radiative transfer in coupled media like the atmosphere-ocean system," AIP Conf. Proc. **1531**, 923–926 (2013).
15. B. Hamre, S. Stamnes, K. Stamnes, and J. J. Stamnes, "A versatile tool for radiative transfer simulations in the coupled atmosphere-ocean system: introducing AccuRT," in *Ocean Optics XXII*, Portland, ME, Oct. 26–31, 2014.
16. Z. Lin, S. Stamnes, Z. Jin, I. Laszlo, S. Tsay, W. Wiscombe, and K. Stamnes, "Improved discrete ordinate solutions in the presence of an anisotropically reflecting lower boundary: upgrades of the DISORT computational tool," J. Quant. Spectrosc. Radiat. Transf. **157**, 119–134 (2015).
17. F. X. Kneizys, L. W. Abreu, G. P. Anderson, J. H. Chetwynd, E. P. Shettle, A. Berk, L. S. Bernstein, D. C. Roberson, P. Acharya, L. S. Rothman, J. E. A. Selby, W. O. Gallery, and S. A. Clough, "The MODTRAN2/3 report and LOWTRAN 7 model," F19628-91-C-0132 (Phillips Laboratory, 1996).
18. Z. Ahmad, B. A. Franz, C. R. McClain, E. J. Kwiatkowska, J. Werdell, E. P. Shettle, and B. N. Holben, "New aerosol models for the retrieval of aerosol optical thickness and normalized water-leaving radiances from the SeaWiFS and MODIS sensors over coastal regions and open oceans," Appl. Opt. **49**, 5545–5560 (2010).
19. J. Wei, Z. P. Lee, N. Pahlevan, and M. Lewis, "Transmittance of upwelling radiance at the sea surface measured in the field," Proc. SPIE **9261**, 926105 (2014).
20. R. M. Pope and E. S. Fry, "Absorption spectrum (380-700 nm) of pure water, II, Integrating cavity measurements," Appl. Opt. **36**, 8710–8723 (1997).
21. L. Kou, D. Labrie, and P. Chylek, "Refractive indices of water and ice in the 0.65 m to 2.5 m spectral range," Appl. Opt. **32**, 3531–3540 (1993).
22. A. Morel, "Optical properties of pure water and pure seawater," in *Optical Aspects of Oceanography*, N. G. Jerlov and E. S. Nielson, eds. (Academic, 1974), pp. 1–24.
23. K. Ruddick, "DUE coastcolour round robin protocol, version 1.2," in *Coastalcolour Round Robin*, 2010.
24. A. Bricaud, A. Morel, M. Babin, K. Allali, and H. Claustre, "Variations in light absorption by suspended particles with chlorophyll concentration in oceanic (case 1) waters: analysis and implications for bio-optical models," J. Geophys. Res. **103**, 31033–31044 (1998).
25. H. Loisel and A. Morel, "Light scattering and chlorophyll concentration in case 1 waters: a re-examination," Limnol. Oceanogr. **43**, 847–858 (1998).
26. G. Fournier and J. L. Forand, "Analytic phase function for ocean water," Proc. SPIE **2258**, 194–201 (1994).
27. C. D. Mobley, L. K. Sundman, and E. Boss, "Phase function effects on oceanic light fields," Appl. Opt. **41**, 1035–1050 (2002).
28. W. Li, K. Stamnes, R. Spurr, and J. J. Stamnes, "Simultaneous retrieval of aerosols and ocean properties: a classic inverse modeling approach II. SeaWiFS case study for the Santa Barbara channel," Int. J. Remote Sens. **29**, 5689–5698 (2008).
29. M. Babin, A. D. Stramski, G. M. Ferrari, H. Claustre, A. Bricaud, G. Obelesky, and N. Hoepffner, "Variations in the light absorption coefficients of phytoplankton, nonalgal particles and dissolved organic matter in coastal waters around Europe," J. Geophys. Res. **108**, 3211 (2003).
30. M. Babin, A. Morel, V. Fournier-Sicre, F. Fell, and D. Stramski, "Light scattering properties of marine particles in coastal and open ocean waters as related to the particle mass concentration," Limnol. Oceanogr. **48**, 843–859 (2003).
31. T. L. Petzold, "Volume scattering functions for selected ocean waters," Technical Report SIO 7278 (Scripps Institute of Oceanography, 1972).
32. C. D. Mobley, *Light and Water: Radiative Transfer in Natural Waters* (Academic, 1994).
33. Y. X. Hu, B. Wielicki, B. Lin, G. Gibson, S. C. Tsay, K. Stamnes, and T. Wong, "Delta-fit: A fast and accurate treatment of particle scattering phase functions with weighted singular-value decomposition least squares fitting," J. Quant. Spectrosc. Radiat. Transf. **65**, 681–690 (2000).
34. L. Fan, W. Li, A. Dahlback, J. J. Stamnes, S. Stamnes, and K. Stamnes, "New neural-network-based method to infer total ozone column amounts and cloud effects from multi-channel, moderate bandwidth filter instruments," Opt. Express **22**, 19595–19609 (2014).
35. IOCCG, "Remote sensing of inherent optical properties: Fundamentals, tests of algorithms, and applications," Reports of the International Ocean-Colour Coordinating Group, No. 5, Z. P. Lee, ed., 2006.
36. K. Stamnes, W. Li, Y. Fan, N. Chen, J. J. Stamnes, A. Folkestad, and K. Sørensen, "The Coastcolour Round Robin (CCRR) algorithm intercomparison," Preliminary report, 2011, ftp://ccrropen@ftp.coastcolour.org/RoundRobin/CCRR_report_OCSMART.pdf.
37. J. E. O'Reilly, S. Maritorena, B. G. Mitchell, D. A. Siegel, K. L. Carder, S. A. Garver, M. Kahru, and C. McClain, "Ocean color chlorophyll algorithm for SeaWiFS," J. Geophys. Res. **103**, 24937–24953 (1998).
38. K. J. Voss and A. L. A. Chapin, "An upwelling radiance distribution camera system, NURADS," Opt. Express **13**, 4250–4262 (2005).